

Depth capabilities of neutron and synchrotron diffraction strain measurement instruments. I. The maximum feasible path length

Philip John Withers

Manchester Materials Science Centre, Grosvenor Street, Manchester M1 7HS, UK. Correspondence e-mail: philip.withers@man.ac.uk

In this paper an algorithm is presented for estimating the maximum feasible penetration path length for neutron and synchrotron X-ray strain measurement instruments. This reflects the attenuation and scattering capability of the material under examination, the incident flux and detector arrangement, the likely background signal, the required strain measurement accuracy, the sampling volume and the diffracting geometry. Its validity and generality is examined through a consideration of data collected using a number of instruments on a variety of materials. Two criteria for the maximum feasible path length are examined: one based on the maximum acquisition time, the other based on the minimum acceptable peak height to background ratio. As demonstrated in the companion paper [part II: Withers (2004). *J. Appl. Cryst.* **37**, 607–612], the algorithm can be used to delineate those conditions under which neutron and synchrotron X-ray radiations can provide useful information and to identify which is most suited to any particular measurement task.

© 2004 International Union of Crystallography
Printed in Great Britain – all rights reserved

1. Introduction

Since access to neutron and synchrotron X-ray facilities is limited, one needs to consider the advantages of these methods over existing, more readily available and cheaper strain measurement techniques very carefully. Their unique selling point over other methods is the ability to provide residual strain information as a function of depth non-destructively. As a result, it is useful to consider the depth limitations for these radiations from the viewpoint of undertaking strain measurement. Normally the desired strain measurement accuracy is specified or predetermined by the engineering problem of interest. The largest allowable sampling gauge volume is determined by the spatial resolution required and the question is then how long will it take to make a measurement at a given depth, and how deep can measurements be made before they become prohibitively time-consuming? Furthermore, it is advisable to ask whether the task is better suited to laboratory X-rays, neutrons or synchrotron X-rays. Of course, in practice the answers to these questions are partly sample dependent and partly instrument dependent.

Sample-dependent effects often play an important role in determining whether it is practical to make a strain measurement. These effects include grain size, prior plastic work and texture effects. Such factors have been studied in some detail previously and will be covered only briefly here. Grain size and the degree of crystal perfection determine the mosaic size (Hirsch, 1956), which in turn influences the minimum practical sampling volume for which conventional

powder diffraction methods of analysis can be applied. Powder methods need a large number of individual diffracting regions. Whether this condition is met is a complex function of grain size, plastic work, incident-beam divergence and the angular discrimination of the detector (Andrews & Johnson, 1959). Furthermore, these factors also affect the onset of primary and secondary extinction, which can limit the relative strengths of the incident and diffracted beams (Sears, 1989). In this paper, it is assumed that the sample is sufficiently fine grained that powder methods can be applied. The crystallographic texture is a measure of the degree to which the grains in a polycrystalline sample are not randomly oriented. Since manufacturing processes generally involve plastic deformation, and this has the effect of modifying the crystallographic orientation of the grains, engineering components are often textured to some extent. This can have a very strong effect on the strength of a given *hkl* diffraction peak measured in a particular direction. As a result, the peak may, in certain circumstances, vary by two or three orders of magnitude according to the measurement direction. The study of crystallographic texture is a well developed field with many applications in materials science which have been dealt with recently in the textbook by Kocks *et al.* (1998). This aspect will not be covered in this paper and it will be assumed that the material is untextured. In cases where there is strong texture, it may not be feasible to measure some peaks at the feasible path lengths calculated in this paper, but on the other hand this means that other peaks will probably be more intense than these simple estimates would suggest. Finally, at certain special wavelengths, incident-beam penetration may vary sharply due to

Table 1

Approximate attenuation lengths (l_μ) (mm) for investigation by laboratory X-rays, synchrotron X-rays [Ellemaume (1999) using an approach described by Chapman *et al.* (1988)] and neutrons (Hutchings & Windsor, 1987).

	Energy (keV)	Wavelength (Å)	Approximate attenuation length (l_μ) (mm)				
			Al	Ti	Fe	Ni	Cu
Thermal neutrons	2.5×10^{-5}	1.80	96	18	8	5	10
ID 15 (ESRF)	150	0.08	39	14	7	5	5
ID 31 (ESRF)	60	0.21	13	3	1.1	0.8	0.7
ID 11 (ESRF)	49	0.25	10	2	0.7	0.5	0.4
BM16 (ESRF)	38	0.32	6.5	1	0.4	0.2	0.2
16.3 SRS	31	0.40	3.3	0.5	0.16	0.11	0.10
Laboratory (Cu $K\alpha$)	8.05	1.54	0.076	0.011	0.004	0.023	0.021

the influence of Bragg edges. These sharp increases in transmission occur at wavelengths which just exceed twice the lattice spacing of important reflections in the polycrystal. At this point, the Bragg condition reaches 180° and Bragg diffraction is no longer possible for that reflection, causing the transmissivity to increase sharply (Santisteban *et al.*, 2001).

The above material-dependent factors mean that it is not possible to predict the diffracted signal precisely in any given situation without a detailed knowledge of the material's microstructure. Only rarely is all this microstructural information available; nevertheless, a general means of checking out what is likely to be practicable prior to costly experimentation and characterization is required. In this paper, a simple rigorous approach for calculating the maximum feasible path length is presented based on instrumental characteristics and engineering requirements, such that the best approach can be identified. It utilizes the expression for the uncertainty in diffraction peak position given by Withers *et al.* (2001). It is a systematic extension of the empirical concept of the maximum economic thickness developed by Webster, Wang *et al.* (1996) specifically for neutron diffraction.

As discussed in part II (Withers, 2004), the power of the method lies in providing a benchmark for estimating the feasibility of running specific experiments on a given instrument. It provides a way to make reasoned choices and to compare different measurement strategies. In addition, it provides a framework for optimizing and monitoring the performance of existing, or for designing new, strain measurement instruments.

2. Attenuation length as a guide to penetration depth

Of course, one of the most important parameters governing the maximum feasible depth at which measurements can be made is the extent of attenuation with path length. It is a simple matter to calculate the thickness of a given material that will attenuate 63% of the incident beam (see Table 1), called here the attenuation length (l_μ). It has long been realised that the large attenuation lengths of neutrons relative to laboratory X-rays gives them advantages for measurements deep within engineering materials. It is also evident from Table 1 that at energies in excess of 150 keV, the attenuation lengths of X-ray photons are comparable with neutrons for many materials.

While the attenuation length gives an indication of the maximum depth/thickness from which it is feasible to obtain information for a given material, this does not provide the complete picture. On the whole, fluxes at neutron sources are orders of magnitude lower than laboratory X-ray photon fluxes, while synchrotron X-ray sources are orders of magnitude more intense. As a result, it may be possible to accept lower transmission probabilities, because the detected signal may still be comparable. Furthermore, the diffracting angles, typical background levels, detector configurations, sampling gauge volumes and peak widths characteristic of X-ray, synchrotron X-ray and neutron diffraction are quite different, making side-by-side comparisons difficult. As a result, it is important to consider the diffracted signal necessary for achieving the desired strain measurement accuracy and the rate at which it is attained. That is the purpose of this paper. The consequences for real experiments and instruments are investigated in part II.

3. The necessary signal

3.1. Negligible background

Clearly, the number of diffracted particles that must be detected (the total acquired signal N) depends on the required measurement accuracy. Furthermore, a lower signal is required to determine the position of a narrow diffraction peak than a broad one. In order to establish the maximum useful depth of penetration, a quantitative relationship is required between the stipulated strain measurement uncertainty $\text{Err}(\varepsilon)$ and the necessary signal.

The elastic strain ε is determined from the shift in the position of the diffraction peak either in terms of the diffracting angle (in radians) $(\theta - \theta_0)$ or wavelength $(\lambda - \lambda_0)$ according to whether a monochromatic beam or a white beam is used, where θ_0 and λ_0 are the corresponding unstrained values:

$$\text{monochromatic } \varepsilon = -\cot \theta (\theta - \theta_0) \quad (1a)$$

and

$$\text{white beam } \varepsilon = (\lambda - \lambda_0)/\lambda, \quad (1b)$$

from which uncertainty in strain is given by

$$\text{Err}(\varepsilon)^2 = \text{Err}(d)^2/d^2 + \text{Err}(d_0)^2/d_0^2, \quad (2)$$

where d and d_0 are the strained and strain-free lattice parameters and $\text{Err}(d)$ and $\text{Err}(d_0)$ their respective uncertainties. It then follows that if d and d_0 are very similar, which they always are, and their uncertainties are also similar, then the strain uncertainty is proportional to the uncertainty in d . In practice, the shift in lattice spacing is determined by fitting the diffraction peak to a Gaussian profile or other suitable functional form. Using the approach outlined by de Sivia (1996), it has been shown that when the background is negligible these wavelength or angular shifts can be determined to a precision of $\text{Err}(\lambda)$ or $\text{Err}(\theta)$, respectively, where (Withers *et al.*, 2001)

$$\text{Err}(\lambda)^2 = u_\lambda^2/N \quad \text{or} \quad \text{Err}(\theta)^2 = u_\theta^2/N, \quad (3)$$

where u is the standard deviation of the peak profile in λ or θ , and N is the integrated neutron or photon count. The validity of this relation has been shown for a range of experimental data by Webster & Kang (2002).

Combining equations (1) and (3), the uncertainty in ε is given by

$$\text{Err}(\varepsilon) = u_\lambda/[\lambda(N^{1/2})] \quad \text{or} \quad \text{Err}(\varepsilon) = u_\theta \cot \theta/(N^{1/2}). \quad (4)$$

We shall see that for the conditions characteristic of neutron diffraction, the number of counts required to achieve 1×10^{-4} strain uncertainty at $2\theta = 90^\circ$ on a peak of full width at half-maximum 0.7° (in 2θ), an integrated signal of around 650 counts is required (Table 4). For synchrotron X-ray sources, the very narrow peak widths [e.g. $\sim 0.01^\circ$ (in 2θ) for ID31 at the ESRF] mean that in theory very few photons are required to achieve 10^{-4} strain accuracy (see Table 4). In practice, one would probably wish to have a somewhat larger number of integrated counts, but certainly at least an order of magnitude less than required to achieve the same accuracy relative to neutron sources.

From equation (4), the time (t) required to achieve a given strain uncertainty is

$$t \simeq u_\lambda^2/[\lambda^2 \text{Err}(\varepsilon)^2 n] \quad \text{or} \quad t \simeq \cot^2 \theta u_\theta^2/[\text{Err}(\varepsilon)^2 n], \quad (5)$$

where n is the integrated diffraction peak count recorded per unit time ($N = nt$).

3.2. Significant background

Increasing levels of background increase the signal required to achieve a given accuracy (Withers *et al.*, 2001). This becomes increasingly important when making measurements at depth because of the long data acquisition times associated with weak signals, which mean that background levels can be significant. It has been shown analytically for Gaussian peak shapes that, for the same integrated diffraction peak count, the strain uncertainty increases by a penalty factor $[1 + 2(2^{1/2})B/H^{hkl}]$, where H^{hkl} is the height of the hkl peak and B the background level (note that $H^{hkl} = h^{hkl}t$, $B = bt$) (Withers *et al.*, 2001):

$$\begin{aligned} \text{Err}(\varepsilon) &= u_\lambda/\lambda\{N/[1 + 2(2^{1/2})b/h^{hkl}]\}^{1/2} \quad \text{or} \\ \text{Err}(\varepsilon) &= \cot \theta u_\theta/\{N/[1 + 2(2^{1/2})b/h^{hkl}]\}. \end{aligned} \quad (6)$$

Alternatively, the time t to achieve the same accuracy increases by the penalty factor $[1 + 2(2^{1/2})b/h^{hkl}]$:

$$\begin{aligned} t &= u_\lambda^2[1 + 2(2^{1/2})b/h^{hkl}]/n \text{Err}(\lambda)^2 \quad \text{or} \\ t &= u_\theta^2[1 + 2(2^{1/2})b/h^{hkl}]/n \text{Err}(\theta)^2, \end{aligned} \quad (7)$$

or

$$\begin{aligned} t &\simeq [1 + 2(2^{1/2})b/h^{hkl}]u_\lambda^2/[\lambda^2 \text{Err}(\varepsilon)^2 n] \quad \text{or} \\ t &\simeq [1 + 2(2^{1/2})b/h^{hkl}]u_\theta^2 \cot^2 \theta/[\text{Err}(\varepsilon)^2 n]. \end{aligned} \quad (8)$$

A large body of experimental strain measurement data has been collected for a round-robin study as part of the VAMAS TWA20 neutron strain measurement standardization project. The experimentally determined uncertainties are plotted against the diffracted peak height to background ratio in Fig. 1. From an experimental perspective, it is interesting to note that the facilities have recorded data with a very broad spectrum of diffracted signal to background ratios (from 0.3 to 85). Despite the scatter in the data, the data are broadly in agreement with equation (6).

4. Instrument performance

In this section, a method for obtaining performance indicators for neutron strain and synchrotron strain measurement instruments is presented. Throughout this paper, this analysis is applied, for illustrative purposes, to a generic neutron instrument (based on the NRU L3 instrument at Chalk River) and a variety of synchrotron instruments having different

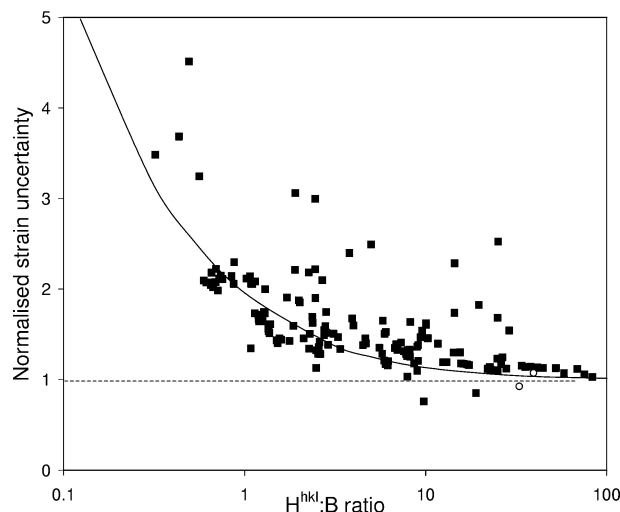


Figure 1 The measured uncertainties normalized against equation (4) for round-robin measurements on the two phases of an $\text{Al}_2\text{O}_3/\text{SiC}$ nanocomposite sample performed by many neutron facilities across the world as part of the VAMAS TWA20 standardization exercise (all data fitted by E. C. Oliver) (Webster, 2001). Squares represent neutron data; open circles represent synchrotron data. The solid curve represents the function $[1 + 2(2^{1/2})b/h^{hkl}]^{1/2}$.

Table 2

Macroscopic cross sections (mm⁻¹) for various engineering materials calculated on the basis of the same databases as Table 1.

Note that $l_\mu = (\Sigma_{\text{coh}} + \Sigma_{\text{incoh}} + \Sigma_{\text{absorb}})^{-1}$. Σ_{photo} is the cross section for creating a photoelectron and is analogous to Σ_{absorb} for neutrons.

	Energy (keV)	Σ	Al	Ti	Fe	Ni	Cu
Neutron	1×10^{-5}	Σ_{coh}	0.009	0.0077	0.0971	0.1218	0.0634
		Σ_{incoh}	0.00005	0.0151	0.0033	0.0475	0.0044
		Σ_{absorb}	0.00139	0.0345	0.0217	0.0410	0.03202
ID15	150	Σ_{coh}	0.00152	0.0053	0.0125	0.0167	0.01707
		Σ_{incoh}	0.03451	0.0536	0.0934	0.109	0.10493
		Σ_{photo}	0.001	0.014	0.046	0.069	0.074
ID31	60	Σ_{coh}	0.009	0.030	0.069	0.092	0.094
		Σ_{incoh}	0.040	0.061	0.107	0.123	0.118
		Σ_{photo}	0.026	0.250	0.760	1.117	1.194
ID11	49	Σ_{coh}	0.012	0.041	0.095	0.126	0.129
		Σ_{incoh}	0.041	0.061	0.106	0.123	0.117
		Σ_{photo}	0.047	0.435	1.304	1.920	2.050
BM16	40	Σ_{coh}	0.018	0.061	0.139	0.185	0.189
		Σ_{incoh}	0.041	0.061	0.105	0.122	0.116
		Σ_{photo}	0.096	0.857	2.54	3.74	3.96
SRS	31	Σ_{coh}	0.029	0.098	0.22	0.294	0.3
		Σ_{incoh}	0.040	0.059	0.10	0.12	0.11
		Σ_{photo}	0.237	2.03	5.95	8.7	9.2
X-ray (Cu $K\alpha$)	8.05	Σ_{coh}	0.20	0.52	1.19	1.61	1.66
		Σ_{incoh}	0.03	0.04	0.06	0.06	0.06
		Σ_{photo}	12.9	89.9	235	41.33	44.85
Density (g cm ⁻³)			2.698	4.508	7.873	8.907	8.933
Atomic weight			26.98	47.9	55.85	58.71	63.54

energies (60, 50, 40 and 30 keV). Unless specifically mentioned, it is assumed that the sampling gauge for neutrons is 40 mm³ and that for the synchrotron instruments is 1 mm³. The characteristic Bragg angles (θ) and peak widths (standard deviation u_θ) assumed in the calculations are summarized in Table 4.

4.1. The detected signal

While instruments are often compared in terms of their incident flux, it is not always the case that the highest flux instruments acquire data at the fastest rates. Often, medium-flux instruments can out-perform high-flux instruments through having a more efficient detector arrangement.

In estimating the maximum feasible depth from which strain information can be obtained, *i.e.* the maximum depth beyond which it is not really practical to measure, one needs to estimate the signal detected as a function of depth. If we consider, for simplicity, a small cuboidal gauge cross section,¹ then the detected signal varies according to the incident flux, the detector arrangement, gauge volume, scattering material and the scattering geometry. Of the N_0 particles passing through the incident slit and incident on the sample, the number of particles diffracted, $N_{\text{diff}}^{\text{hkl}}$, from the sampling gauge volume, $V_v = A_v L_v$, involving a total path length l through the material of interest, is given by

¹ Provided that the gauge dimension along the beam direction is significantly shorter than the attenuation length, the scattered signal is dependent only on the sampling volume V_v , independent of the gauge shape; otherwise the level of scattering is shape dependent. This can be important especially when considering X-rays, in which case V_v can be replaced by V_{eff} to account for attenuation within the gauge. In the following discussion, it is the sampling volume rather than the shape which is important.

$$N_{\text{diff}}^{\text{hkl}} = N_0 P_{\text{transmit}}(l) P_{\text{diff}}^{\text{hkl}} L_v = \Phi t A_v \exp(-\mu l) P_{\text{diff}}^{\text{hkl}} L_v, \quad (9)$$

where A_v is the area of the incident slit, μ is the linear absorption (attenuation) coefficient, Φ is the incident flux per unit area, t is the data acquisition time (s) and N_0 is the number of particles incident on the sample, given by $\Phi t A_v$. $P_{\text{transmit}}(l)$ is the fraction of the incident signal transmitted a distance l through the material and $P_{\text{diff}}^{\text{hkl}} dl$ is the probability that a neutron/photon is diffracted on travelling a distance dl so that the probability of a particle being diffracted within the sampling gauge length is approximately $P_{\text{diff}}^{\text{hkl}} L_v$. In the above relation, it is assumed that the probability of scattering or absorption over the sampling length L_v is small¹ (*i.e.* $L_v \ll l_\mu$). Equation (9) can be reformulated in terms of the scattering by each scattering site. The atomic σ_{coh} and the macroscopic Σ_{coh} cross sections (see Table 2) for coherent scattering are related by the total number of atoms per unit volume, $n_{\text{atoms}} N_c$:

$$\Sigma_{\text{coh}} = n_{\text{atoms}} N_c \sigma_{\text{coh}} = (1/v_0) \sigma_{\text{coh}}, \quad (10)$$

where N_c is the number of unit cells/volume, n_{atoms} is the number of atoms per cell and v_0 is the average volume per atom. As a result, the total probability of a particle being diffracted by the sample taking into account all hkl , P_{diff} , is given by $\Sigma_{\text{coh}} L_v$. For a single hkl reflection (Bacon, 1975),

$$P_{\text{diff}}^{\text{hkl}} = \frac{\lambda^3}{4n_{\text{atoms}}^2 v_0^2} \frac{m^{\text{hkl}} F^{\text{hkl}2}}{\sin^2 \theta_{\text{B}}^{\text{hkl}}}, \quad (11)$$

where $\theta_{\text{B}}^{\text{hkl}}$ is the Bragg angle for the hkl reflection, $F^{\text{hkl}2}$ the structure amplitude factor per unit cell, and m^{hkl} the multiplicity. For a simple metal, $F^{\text{hkl}2}$ can be replaced by $M^{\text{hkl}} b^2$, where $b = (\sigma_{\text{coh}}/4\pi)^{1/2}$ is the coherent scattering length for the element, or the effective scattering length representing the

constituent elements in a disordered alloy, and M^{hkl} describes the way the wavelets from atoms within the unit cell superpose and is crystal structure dependent. In which case, $F^{hkl2} = M^{hkl} v_0 \Sigma_{\text{coh}} / 4\pi$.

Of course, not all diffracted particles are collected by the detector since it will occupy only a fraction of the total solid angle Ω . If the detector having efficiency $\%_{\text{detect}}$ is l_{detect} high and at a distance r from the sample, then the fraction of particles diffracted from V_v towards, and detected by, the detector if correctly positioned at θ_B^{hkl} is given by

$$P_{\text{detect}}(\theta)2\Delta\theta = \%_{\text{detect}} \frac{l_{\text{detect}}}{2\pi r \sin 2\theta_B^{hkl}} \delta(2\theta_B^{hkl} - 2\theta), \quad (12)$$

where δ is the Kronecker delta. In reality the diffracted signal is not all diffracted at θ_B^{hkl} . Instead, the Kronecker delta function could more realistically be replaced by a Gaussian profile of standard deviation $2u_\theta$ in 2θ :

$$P_{\text{detect}}(\theta)2\Delta\theta = \%_{\text{detect}} \frac{l_{\text{detect}}}{2\pi r \sin 2\theta_B^{hkl}} \times \left\{ \frac{1}{2u_\theta(2\pi)^{1/2}} \exp\left[-\frac{(\theta - \theta_B)^2}{2u_\theta^2}\right] \right\} 2\Delta\theta. \quad (13)$$

This means that the number of diffracted particles detected by a single detector, or detector bin of a position-sensitive detector (PSD), of angular width $2\Delta\theta$ is given by

$$\begin{aligned} N_{\text{detect}}^{hkl}(2\Delta\theta) &= \Phi t A_v P_{\text{transmit}}(l) P_{\text{diff}}^{hkl} L_v P_{\text{detect}}(\theta) 2\Delta\theta \\ &= (\Phi t A_v) [\exp(-\mu l)] \left[\frac{\lambda^3 m^{hkl} F^{hkl2}}{4n_{\text{atoms}}^2 v_0^2 \sin^2 \theta_B^{hkl}} \right] L_v \\ &\quad \times \left\{ \%_{\text{detect}} \frac{l_{\text{detect}}}{2\pi r \sin 2\theta_B^{hkl}} \frac{1}{2u_\theta(2\pi)^{1/2}} \right. \\ &\quad \left. \times \exp\left[-\frac{1}{2} \frac{(\theta - \theta_B)^2}{u_\theta^2}\right] \right\} 2\Delta\theta. \end{aligned} \quad (14)$$

It is worthwhile to consider the use of a PSD and a serial detector separately for a moment. For a serial detector, the effective angular width of the detector ($2\Delta\theta_{\text{detect}}$) is not obvious to the user, who is more concerned with the angular measurement interval ($2\Delta\theta_{\text{bin}}$) and the time to measure a point t_{pt} . The total measurement time then becomes $t = t_{\text{pt}} n_{\text{pts}}$, where n_{pts} is the number of points recorded. However, since a serial detector has a fractional angular coverage of only $2\Delta\theta_{\text{detect}}/2\Delta\theta_{\text{scan}}$ of the total scan, its performance in collecting the whole peak can simply be corrected by multiplying the efficiency by this factor (for a PSD this factor equals 1):

$$\begin{aligned} P_{\text{detect}} &= \%_{\text{detect}} \frac{l_{\text{detect}}}{2\pi r \sin 2\theta_B^{hkl}} \frac{2\Delta\theta_{\text{detect}}}{2\Delta\theta_{\text{scan}}} \\ &= \%_{\text{detect}}' \frac{l_{\text{detect}}}{2\pi r \sin 2\theta_B^{hkl}} \frac{1}{2\Delta\theta_{\text{scan}}}. \end{aligned} \quad (15)$$

In a sense, the serial detector can be thought of as an inefficient PSD and we can incorporate $2\Delta\theta_{\text{detect}}$ into the efficiency term $\%_{\text{detect}}'$. For neutrons F^{hkl2} is independent of θ , while for

X-rays it varies considerably with angle. For simplicity, let us model the scattering factor for X-rays as

$$F^{hkl} = F_0^{hkl} \{6^{-\sin\theta/\lambda} + (A/200)[1 - \exp(-\sin\theta/\lambda)]\} \quad (16)$$

(with λ in \AA), A representing atomic number and F_0^{hkl} the scattering for $\theta = 0$. While less accurate than conventional polynomial forms (Krawitz, 2001), the error is considerably less than 20% over the whole range of θ for Al and Cu, and most materials between, and avoids the need for look-up tables and element-specific coefficients.

4.2. The instrumental detected flux constant

In the expression for the detected count integrated over the diffracted peak, N_{detect}^{hkl} , ΦP_{detect} concerns the instrument and $V_v P_{\text{transmit}}(l) P_{\text{diff}}^{hkl}$ is sample dependent. Since

$$\Phi P_{\text{detect}} = \Phi \%_{\text{detect}}' \frac{l_{\text{detect}}}{2\pi r \sin 2\theta_B^{hkl}} \frac{1}{2\Delta\theta_{\text{scan}}}, \quad (17)$$

we can characterize the performance of the instrument by grouping together the fixed terms to define an instrumental flux constant Φ_{instr} :

$$\Phi_{\text{instr}} = \Phi \%_{\text{detect}}' \frac{l_{\text{detect}}}{2\pi r} = \Phi \%_{\text{detect}} \frac{l_{\text{detect}}}{2\pi r} 2\Delta\theta_{\text{detect}}, \quad (18a)$$

of which Φ , l_{detect} , $\%_{\text{detect}}$ and $2\Delta\theta_{\text{detect}}$ are difficult to quantify, but Φ_{instr} can also be expressed using equation (14) as

$$\Phi_{\text{instr}} = \left[\frac{N_{\text{detect}}^{hkl}}{V_{\text{eff}} t} \frac{4n_{\text{atoms}}^2 v_0^2 \sin^2 \theta_B^{hkl} \sin 2\theta_B^{hkl}}{\lambda^3 m^{hkl} F^{hkl2} \exp(-\mu l)} \right] 2\Delta\theta_{\text{scan}}, \quad (18b)$$

all of which can be measured.

Here the sampling volume V_v has been replaced by the effective sampling volume V_{eff} . This is because the scattering is not strictly proportional to V_v . V_{eff} takes into account two factors: firstly the attenuation across the gauge volume, which means that the whole volume is not illuminated to the same extent, and secondly, the fact that the gauge may only be partially filled. V_{eff} would equal V_v if the attenuation coefficient were negligible. One way of establishing the detected flux constant for a given instrument is simply to use published instrumental flux data along with measurements/estimates of detector efficiency and capture angles using equation (18a). However, these parameters are often either unavailable or unreliable. A more pragmatic approach is to use a standard calibration sample to evaluate the term experimentally using equation (18b). Another useful benchmark is $n_{\text{Al}}^{311}(x)$, the number of particles that would be detected in normal reflecting geometry from 1 mm^3 of Al (311) in 1 s at a depth x .

4.3. Determination of instrumental constants

Since the effect of background is important in determining instrument performance, rather than employ a small instrument calibration sample, it was decided to use surface scans in reflection geometry on standard test blocks to determine the representative detected flux constant for various instruments. One such surface scan is shown in Fig. 2. A number of important well known characteristic features of the intensity

Table 3

Preliminary values of the instrumental detected flux, Φ_{instr} , and the background constants, β_0 , β_{sample} , extracted from entrance curves in reflection geometry.

The particle count rates b_0 , b_{sample} , b_{incoh} , $n_{\text{Al}}^{311}(0)$ and h_{Al}^{311} correspond to the various background and signal components that would be recorded in reflection in 1 s for 1 mm³ (40 mm³ for neutrons) sampling volume of Al at the surface. The peak profile constants expressed in counts can be converted to counts/degree by dividing by the bin width ($2\Delta\theta_{\text{bin}}$).

	$2\Delta\theta_{\text{bin}}$ ($^\circ$)	Φ_{instr} (counts m ⁻² s ⁻¹)	β_0 (counts m ⁻² s ⁻¹)	β_{sample} (counts m ⁻² s ⁻¹)	b_0 (counts s ⁻¹)	$b_{\text{sample}}(0)$ (counts s ⁻¹)	$b_{\text{incoh}}(0)$ (counts s ⁻¹)	$n_{\text{Al}}^{311}(0)$ (counts s ⁻¹)	$h_{\text{Al}}^{311}(0)$ (counts s ⁻¹)	h/b
Neutrons	0.084	2.0×10^6	1×10^5	5×10^6	1×10^{-2}	5×10^{-2}	6×10^{-5}	3	0.4	6
ID31	0.0010	2×10^{10}	3×10^8	3×10^{11}	9	70	0	1000	130	2
ID11	0.0005	5×10^{10}	1×10^8	1×10^{10}	10	9×10^{-1}	0	2300	60	4
BM16	0.0033	8×10^8	4×10^5	2×10^{10}	2×10^{-1}	5	0	50	10	2
16.3	0.0100	7×10^9	3×10^7	1×10^{11}	20	90	0	1000	425	4

curve should be noted. Firstly, the intensity rises initially as more and more of the gauge enters the surface (this is because V_{eff} increases); then the recorded intensity decreases approximately exponentially due to increasing attenuation once the gauge is completely submerged. Less well catalogued in the literature is the variation of the background count which is composed of an approximately constant term and an exponentially decreasing term.

Clearly there are a number of ways in which Φ_{instr} can be extracted from curves such as that in Fig. 2. In reality, the actual value of Φ_{instr} recorded will also vary according to the diffraction peak, or peaks, collected, as well as sample texture, but if a single standard calibration sample is used across a number of instruments, a comparative measure can be obtained. Besides, given the logarithmic dependence of the maximum path length on the instrumental flux and the inexact nature of the calculation, guideline values are sufficient.

Approximate values of Φ_{instr} have been inferred using surface entrance scans similar to that in Fig. 2 (mostly collected for the 311 reflection using a standard Al sample) at a wide range of neutron and synchrotron sources. At a given

instrument, the integrated intensity of the diffraction peak has been determined using the accepted method (scanning detector with or without analyser, PSD, energy-dispersive detector, *etc.*). The values of Φ_{instr} and $n_{\text{Al}}^{311}(0)$ are shown in Table 3 using the data in Table 2; the value of Φ_{instr} recorded using instrument 16.3 at the SRS is large compared with that from BM16 because no analyser crystal was used in the case of the former. In the calculations, the diffraction angles and peak widths summarized in Table 4 were used. Because deep measurements at neutron sources usually involve much larger sampling gauges than are typical either for near-surface neutron or synchrotron X-ray measurements, a neutron sampling gauge of 40 mm³ has been assumed throughout this paper. Note that the integrated diffraction peak count rates at neutron sources are very small [$n_{\text{Al}}^{311}(0) = 3$ neutrons every second for a 40 mm³ sample] whereas for synchrotron instruments they can be 10⁴ times greater for the same sampling volume.

4.4. The characteristic background flux

Equation (6) dictates that the background flux is also an important factor in determining the achievable strain measurement accuracy, especially when the signal is low. Some level of background is unavoidable in that it is related to the scattering capability of the sampling volume and it cannot be removed by analysers. Incoherent neutron scattering from the sampling gauge volume comes into this category. The incoherent neutron scattering from V_v is given by

$$P_{\text{incoh}} L_v = \sum_{\text{incoh}} L_v, \quad (19)$$

which means that the number of incoherently scattered particles detected is

$$N_0 P_{\text{transmit}} L_v P'_{\text{incoh}} P'_{\text{detect}},$$

noting that because the incoherent scattering is isotropic, the probability of capture by the detector (P'_{detect}) is lower than for the diffracted radiation, giving a coherent peak to incoherent background ratio of

$$\begin{aligned} \frac{h^{hkl}}{b_{\text{incoh}}} &= \frac{\lambda^3}{2n_{\text{atoms}}^2 v_0^2} \frac{m^{hkl} F^{hkl2}}{\sin \theta_B^{hkl} \sin 2\theta_B^{hkl} \sum_{\text{incoh}} 2u_\theta(2\pi)^{1/2}} \frac{1}{\sum_{\text{coh}} \lambda^3 m^{hkl} M^{hkl}} \frac{1}{\sum_{\text{incoh}} 8\pi n_{\text{atoms}}^2 v_0 \sin \theta_B^{hkl} \sin 2\theta_B^{hkl} 2u_\theta(2\pi)^{1/2}}. \quad (20) \end{aligned}$$

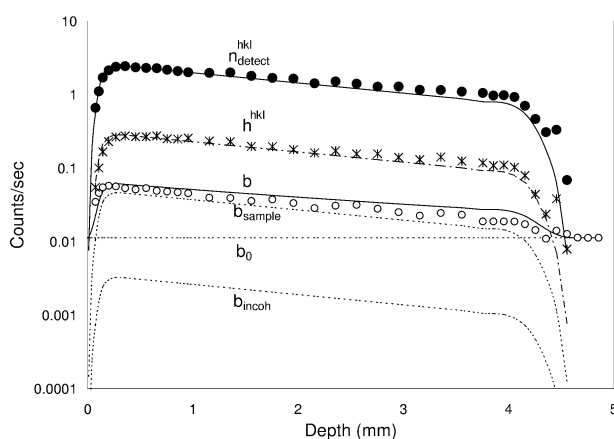


Figure 2

The characteristic integrated (311) peak count rate, n_{detect}^{hkl} (solid circles), peak height, h^{hkl} (crosses), and background rate, b (open circles), as a function of depth upon entering a 4.2 mm thick flat-walled can containing Ni powder measured in reflection at the NRU reactor, Chalk River, Canada, for a $20 \times 0.5 \times 0.5$ mm sampling gauge (Browne, 2001). The sudden rise in diffracted intensity at zero depth and the decrease at 4.2 mm are due to the gauge becoming partially filled. The corresponding model curves are also shown.

In other words, the broader the peak, the poorer the inherent neutron signal to background ratio. It is clear from Fig. 2 that for Ni (indeed for most materials), the incoherent background contribution is small. This is because many other sources of background exist. Air scattering can be significant, especially for synchrotron X-rays, and can enter the detector through the diffracted beam slits unless an analyser crystal is used. At elevated temperatures, scattering into the background arising from the Debye–Waller factor can also be important. Other sources of background include multiple scattering. This can occur within the sampling gauge if L_v/l_μ is large (which it rarely is), or within the component if the sample dimensions are large compared with l_μ (which they often are). An analyser crystal is most effective at precluding the latter.

In this paper, the many sources of background signal which are important at neutron and synchrotron sources are categorized into aperture-independent, sample-dependent and instrument-dependent background components. The first type of background signal is recorded from sources other than the sample, for example from very penetrating particles that can penetrate the shielding around the detector (*e.g.* fast gammas, high-energy X-rays, *etc.*), or electronic noise recorded by a CCD or PSD detector. This is usually a small contribution and is neglected here. The remainder enters the detector through the sampling gauge volume-defining aperture and is dependent on background scattered from the sample and from the local environment. These types of background would tend to zero as the aperture is closed. In order to characterize all the various contributions fully, a comprehensive study would be required before embarking on an experiment. What is needed here is a pragmatic approach which includes the major sources of background in a simple way, enabling estimates of the background to be made without the need for time-consuming experimentation on a case-by-case basis.

Analysis of many strain measurement scans, such as Fig. 2, suggests that the background can be conveniently represented by a constant term which is recorded even when the sampling volume is outside the sample, B_0 ($= b_0 t$), combined with a sample-dependent term. Here both are taken to depend on the detector aperture, in that it is assumed that when the detector slit is closed, no signal is recorded (*i.e.* in many cases aperture-independent scattering can be neglected). The instrument-dependent term, B_0 , should probably be proportional to the detector aperture area; however, to keep the number of parameters to a minimum, it is probably sufficient to make this term $V_v^{2/3}$ dependent. As is evident from Fig. 2, a large component of the background signal varies according to the depth of the sampling volume within the material and decays approximately exponentially with penetration distance. While this includes the incoherent scattering component (B_{incoh}), it is much greater than would be expected from this source alone. The extra contribution, B_{sample} ($= b_{\text{sample}} t$), is probably the result of multiple scattering and has thus been taken here to be proportional to V_v and to $(\Sigma_{\text{coh}} + \Sigma_{\text{incoh}})^2/\Sigma_{\text{tot}}$ (Bacon, 1975). In this way, the overall background count recorded at a given path length for a given material can be well represented by

$$B = B_{\text{incoh}} + B_{\text{sample}} + B_0 = \left\{ \frac{1}{2} \Phi_{\text{instr}} \Sigma_{\text{incoh}} \exp(-\mu l) V_v + \left[\beta_{\text{sample}} \exp(-\mu l) V_v \times \frac{(\Sigma_{\text{coh}} + \Sigma_{\text{incoh}})^2}{\Sigma_{\text{tot}}} \right] + \beta_0 V_v^{2/3} \right\} t \frac{2\Delta\theta_{\text{bin}}}{2\Delta\theta_{\text{scan}}}, \quad (21)$$

where β_{sample} and β_0 are the background constants and $2\Delta\theta_{\text{bin}}$ represents the bin width for both a PSD and a serial detector. Note that here the degradation in the maximum feasible penetration length arising from the incoherent neutron scattering contribution due to an increase in background is predicted to be weaker than the $\Sigma_{\text{coh}}/(\Sigma_{\text{coh}} + \Sigma_{\text{incoh}})$ benchmark figure proposed by Webster, Mills *et al.* (1996). Because the incoherent contribution can be predicted from the instrumental flux and the incoherent scattering cross section, only three parameters (β_0 , β_{sample} and Φ_{instr}) need be determined for any given instrument configuration from the calibration depth scan. Typical values of β_0 , β_{sample} , B_0 , B_{sample} and B_{incoh} are summarized in Table 3.

5. Experimental validation

The preceding sections have defined simple expressions for the variation of diffracted signal and background level as a function of material, diffraction peak, instrumental arrangement and sampling gauge volume and depth, as well as a procedure for establishing the key instrumental constants. The validity of the approach has been tested against a very wide range of neutron and synchrotron instruments and many engineering materials. In Fig. 3, the performance of the algorithms for predicting the integrated count and background levels are shown for the ID31 beamline. The experimental data were collected over a number of visits and the same values of the three instrumental constants were used in all cases. Note the large synchrotron count rates per unit sampling volume compared with the corresponding neutron values in Fig. 2. This means that it is feasible to go to larger multiples of the attenuation length (see part II; Withers, 2004). The fits are sufficient for our purposes (within a factor of 10), given that the primary aim was not to model precisely the diffraction peak and background behaviour; that would require a great deal of information about the sample texture, grain size, *etc.*, and the exact experimental configuration. Instead, the aim was to make acceptable ‘ball-park’ predictions based on just three instrumental parameters and basic materials scattering data. In this way, the measurement capability for a given problem can be estimated *a priori*. Note that beyond a normalized distance of around $l/l_\mu = 6$, the integrated count over the whole peak becomes less than the background signal recorded at a single point; this would be an extreme limit on the maximum depth that can be probed.

6. The maximum feasible path length

Combining equations (6) and (18), the signal needed to achieve a given strain uncertainty $\text{Err}(\varepsilon)$ for a conventional θ – 2θ scan is given by

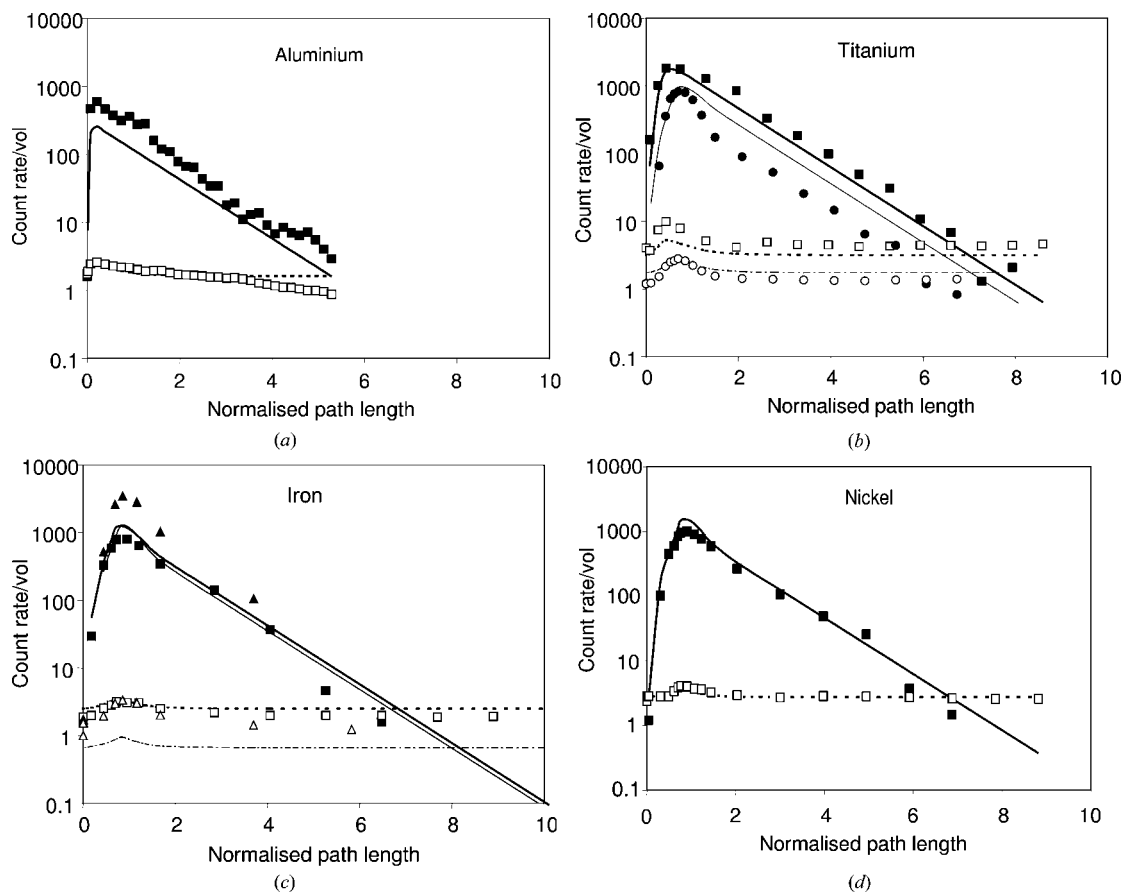


Figure 3

The integrated intensity (solid symbols) and background (open symbols) count rates (normalized by V_v) and the associated predictions (continuous and dashed lines, respectively) for depth scans on (a) Al (311), (b) Ti ($10\bar{1}1$), (c) Fe (200) and (211), and (d) Ni (111) recorded in reflection geometry on ID31 at 60 keV (ESRF). The data represented by square symbols were collected during the same beam period and are modelled by the bolder lines. The other data were collected at various times during the previous 15 months. The Φ_{instr} , β_0 and β_{sample} instrumental parameters were obtained from the Ni data. The path lengths have been normalized by the respective attenuation lengths.

$$N_\varepsilon = \Phi_{\text{instr}} t_\varepsilon V_{\text{eff}} \exp(-\mu l) \frac{\lambda^3}{4n_{\text{atoms}}^2 v^2} \frac{m^{\text{hkl}} F^{\text{hkl}2}}{\sin \theta_{\text{B}}^{\text{hkl}} \sin 2\theta_{\text{B}}^{\text{hkl}} 2\Delta\theta_{\text{scan}}} \\ = \left[1 + 2(2^{1/2}) \frac{b}{h^{\text{hkl}}} \right] \frac{\cot^2 \theta_{\text{B}}^{\text{hkl}} u_\theta^2}{\text{Err}(\varepsilon)^2} \quad (22)$$

where b/h^{hkl} is given by

$$\frac{b}{h^{\text{hkl}}} = \left[\frac{1}{2} \Phi_{\text{instr}} \Sigma_{\text{incoh}} + \beta_0 V_v^{-1/3} \exp(\mu l) + \beta_{\text{sample}} \frac{(\Sigma_{\text{coh}} + \Sigma_{\text{incoh}})^2}{\Sigma_{\text{tot}}} \right] \\ \times \frac{\sin \theta_{\text{B}}^{\text{hkl}} \sin 2\theta_{\text{B}}^{\text{hkl}} 16n_{\text{atoms}}^2 \pi v_0}{\Phi_{\text{instr}} \lambda^3 m^{\text{hkl}} M^{\text{hkl}}} 2u_\theta(2\pi)^{1/2}. \quad (23)$$

Strictly there is no absolute value of the path length beyond which it is not possible to make a measurement to a given accuracy. However, the time required to obtain sufficient diffracted signal relative to the background level becomes uneconomically long as the path length becomes greater. As a result, it is useful to define a maximum feasible path length. At least two criteria can be sensibly used to arrive at such a figure; namely a maximum acceptable time for the taking of a measurement, and a minimum diffracted peak height to background ratio.

6.1. Maximum acceptable acquisition time

The results of the above discussion of strain measurement accuracy can be used to assess the time required, t , to achieve a specified uncertainty, $\text{Err}(\varepsilon)$ from equation (8). This gives the well known result that the acquisition time is inversely proportional to the square of the required uncertainty. In other words, it takes four times as long to achieve twice the strain accuracy. The equation also highlights the need to minimize the background, especially when the signal intensity is low, such as, for example, when making measurements deep within a component.

Inserting equations (22) and (23) into equation (8), we see that the well known observation that the time should increase exponentially with increasing depth is only true for the case of zero background (see the straight line response in Fig. 4). This situation is not at all appropriate for the conditions representative of deep measurements. It is also evident from the figure that were the background to remain constant at the level recorded near the surface, the time to measure to a given strain would be considerably longer than that predicted on the basis of no background. However, in reality, the decreasing level of background observed with increasing depth of the type shown in Fig. 2 means that the actual picture is not so

Table 4

Estimated maximum penetration lengths, l_t , for neutrons and synchrotron sources based on 10^{-4} strain measurement precision and 1 h measurement time, or the penetration length, l_{hib} , at which a signal to background ratio of 1 would be recorded, using the scattering angles and peak widths shown.

Also shown for Al are the time, t_{hib} , at which the l_{hib} criterion is met and the counts necessary to achieve 10^{-4} accuracy in the case of no background, $N_{b=0}$, and at the maximum path length using the 1 h time criterion, N_t . For the neutron data, a sampling gauge volume of 40 mm^3 has been assumed, while a gauge of 1 mm^3 has been used for the synchrotron measurements. Data recorded at the NRU LR3 instrument at Chalk River have been taken as representative of current neutron sources. The times and necessary signals correspond to those for the Al sample.

	θ ($^\circ$)	u_θ ($^\circ$)	Al (311)		Ti (100)		Fe (211)		Ni (311)		Cu (311)		$t_{hib}(\text{Al})$ (min)	$N_{b=0}$	N_t
			l_t	l_{hib}	l_t	l_{hib}	l_t	l_{hib}	l_t	l_{hib}	l_t	l_{hib}			
Webster			237		23		37		21		40				
Neutrons	45	0.147	160	185	22	24	40	43	20	21	36	39	90	650	2000
ID31	8	0.002	115	45	29	16	13	9	8	5	8	5	0.01	3	750
ID11	8	0.004	85	55	19	13	8	6	5	4	5	3	0.2	25	1600
BM16	10	0.004	50	45	9.4	9	4	4	2.5	2.4	2.4	2.3	15	15	90
16.3 SRS	10	0.005	30	20	4.5	3	1	1.5	1.2	0.9	1.1	0.8	0.3	22	900

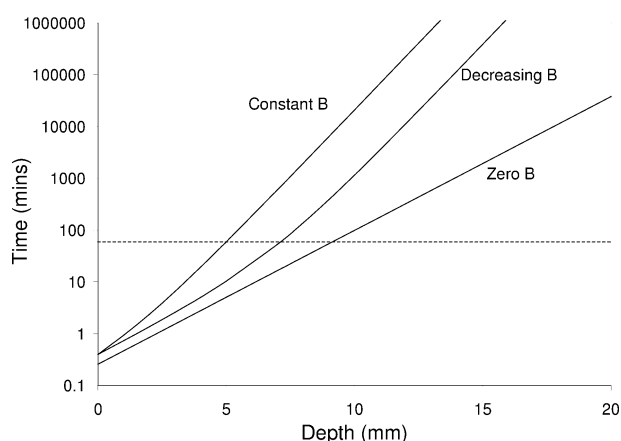


Figure 4
The time needed to attain 10^{-4} strain accuracy in reflection geometry based on representative neutron calibration data (acquired at Chalk River) for a 40 mm^3 Ni gauge volume, with no background, or a background level equal to that recorded near the surface, compared with the decreasing background response predicted from the calibration data (Fig. 2). The 60 min maximum feasible time threshold is marked by the dashed line.

bleak. At shallow depths, the background decreases approximately exponentially at broadly the same rate as the diffracted signal, so that the time to achieve a given strain lies parallel to the zero background limit curve. At larger depths, the constant component of the background level becomes important and the curve remains lower than, but parallel to, the constant background curve (see Fig. 4). For the acquired data, the depths at which 10^{-4} strain uncertainty is achievable in 60 min for a 40 mm^3 Ni gauge are 9.1, 7.0 (see Table 1 of part II) and 5.0 mm for no background, the expected background and that representative of the near-surface, respectively.

In practice, measurement times as long as 24 h have been used for point measurement by neutron diffraction, but this is exceptional. Progressively shorter acquisition times are required for line scans (~ 1 h), area scans (~ 10 min) and volume scans (~ 1 min) because of the increase in the number of measurements (typically ~ 10 , >100 and >500 , respectively) required to complete them. In order to probe larger depths, large sampling volumes are more commonly used for neutron measurements and so, as mentioned earlier, in our calculations

the sampling volume is taken to be 1 mm^3 and 40 mm^3 for synchrotron X-rays and neutrons, respectively. Furthermore, in practice ‘acceptable’ measurement times are not normally as long for synchrotron strain measurements, which are usually of the order of minutes as against hours for neutrons. We will denote the maximum path length for which the required strain accuracy can be achieved in 1 h by l_t . A willingness to accept an acquisition time of 24 h would naturally increase the feasible path length. However, because of the logarithmic scale, increasing the measurement time has only a limited effect on increasing the maximum path length.

The maximum feasible path length under the time-based criteria is obtained by solving a quadratic in $\exp(\mu l)$ with $t = 3600$ s, formed by inserting equation (23) into equation (22). The maximum feasible penetration lengths calculated on the basis of the maximum acceptable time are listed in Table 4. Except for the Al case, these lengths are in startling agreement with the empirical economic thicknesses (x) proposed by Webster (1996) for neutron strain measurements on the basis of practical experience (see Table 4) expressed as

$$b^2 \exp(-\mu x) [\sigma_{\text{coh}} / (\sigma_{\text{coh}} + \sigma_{\text{incoh}})] = 1, \quad (24)$$

where b is the scattering length, and σ_{coh} and σ_{incoh} are the coherent and incoherent cross sections, respectively. The final term in equation (24) was developed largely to account for the practical difficulty associated with measuring at depth when examining Ti samples due to the increased level of background arising from the large incoherent scattering contribution. Without this factor, Webster’s economic thickness for Ti would be ~ 50 mm, which is in excess of that for Fe. The more rigorous incorporation of the effect of the increased incoherent background contribution adopted here automatically captures this effect.

It is instructive to examine the necessary signals, N_t , listed in Table 4. For the generic neutron source, the necessary signal is less than four times that for the ideal case of no background at all ($N_{b=0}$). This is quite acceptable. For the synchrotron instruments, however, the necessary signals are very much larger than the ideal case. This is because the large incident flux allows one to measure at many times the attenuation length, where the peak to background ratio is poor but there is

still sufficient diffracted intensity to measure strain. As a result, large time penalty factors $[1 + 2(2^{1/2})b/h^{hkl}]$ mean that the data acquisition process is very inefficient and it is probably wise to use a signal to background ratio criteria leading to slightly shorter penetration depths, but much faster acquisition times.

6.2. Minimum acceptable signal to background ratio

As we have seen, at large depths the signal tends to become lost in the background. This makes it increasingly time consuming to achieve a specified strain accuracy with increasing depth. One option is to say that beyond a diffraction peak height to background ratio of 1, data acquisition becomes uneconomic, placing a limit of the maximum feasible path length, represented as $l_{h/b}$. This corresponds to an increase in signal of four times that required were there no background at all in order to achieve the same level of uncertainty [equation (6)]. This can be taken as the point at which the time penalty associated with a poorer signal to noise ratio at larger depths starts to become prohibitively steep (see Fig. 5 in part II). The maximum feasible path length under the signal-to-background ratio-based criterion ($h^{hkl}/b = 1$) is obtained directly from equation (23):

$$l_{h/b} = l_{\mu} \ln \left\{ \left[\Phi_{\text{instr}} \frac{\lambda^3}{4v_0^2} \frac{m^{hkl} F^{hkl2}}{\sin^2 \theta_B^{hkl} 2u_{\theta} (2\pi)^{1/2}} - \left\{ \beta_{\text{sample}} \left[\frac{(\Sigma_{\text{coh}} + \Sigma_{\text{incoh}})^2}{\Sigma_{\text{tot}}} \right] + \frac{1}{2} \Phi_{\text{instr}} \Sigma_{\text{incoh}} \right\} \right] \times \frac{1}{\beta_0 V_v^{-1/3}} \right\}. \quad (25)$$

Note that the maximum path length under this criterion does not depend on the specified level of uncertainty, which only determines the necessary acquisition time. The maximum feasible path length can also be considered graphically. In Fig. 5, the variation in background and peak heights per second are shown for Al for various X-ray energy instruments ($V_v = 1 \text{ mm}^3$) and a generic thermal neutron instrument ($V_v = 40 \text{ mm}^3$). The maximum feasible path lengths are shown by the intersection of the height and background curves; under the present conditions, the lengths are summarized in Table 4. The rate at which the peak height develops is 10–1000 times faster for the X-ray instruments than expected for neutron diffraction near the surface for Al (which is a weak neutron scatterer). It is clear from the figure that in the X-ray cases the exponential fall off of the sample background components is considerable and allows measurements to be made to much greater depths than would be the case were the background to remain constant as a function of depth. The absence of an analyser crystal on the SRS (16.3) means that the signal intensity is very high given the relatively low incident flux available, but the background is also high. Despite the low signal to background ratio, the neutron measurements can be made to much larger absolute depths because of the low level of attenuation and the very low background counts. Of course,

as Table 4 shows, the maximum path length is larger for radiations with the larger attenuation lengths. Fig. 5 provides insight into the limitations of current instruments. Under this criterion, the penetration distance is strongly determined by the background constant β_0 . By taking measures to reduce β_0 , the background and peak height curves remain parallel to greater depth and thus the cross-over of the curves is achieved at greater depths, giving better depth capability. Under this criterion, the performance of BM16 at the ESRF is particularly noteworthy, having an especially low β_0 constant and thus being capable of measurements to depths in excess of 7 times the attenuation length, whereas all the other instruments achieve a value of approximately 2–6 times the penetration length.

For neutron sources, this criterion would lead to larger depths than for the 1 h time-limited criterion, but, as Table 4 indicates, the times become prohibitively long and the time-based criterion is probably more appropriate. In contrast, for the synchrotron instruments, the peak to background criterion gives a shorter maximum penetration length. Given that 1 h would be considered an excessively long period to acquire data at a synchrotron source and the time to achieve 10^{-4} accuracy at the $l_{h/b}$ limit is much shorter, this is probably the most appropriate criterion for synchrotron measurements.

7. Conclusions

Of course, the performance capability of a strain measurement instrument is not static. Instrument scientists are always endeavouring to improve strain sensitivity and reduce acquisition times. As a result, the exact values presented here should not be taken too literally. They should be regarded as preliminary values which nevertheless provide useful benchmarks for deciding whether an experiment is feasible on any

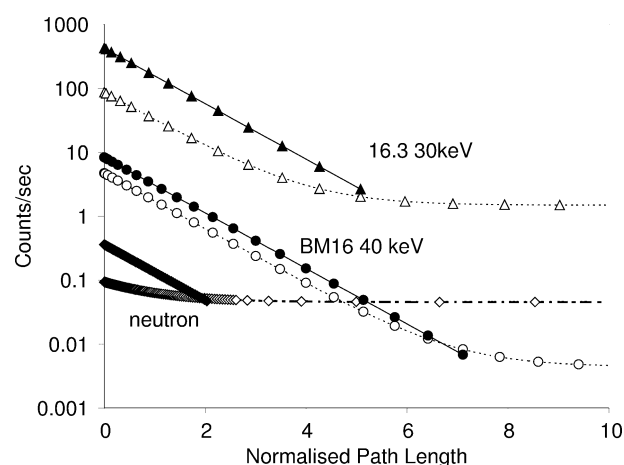


Figure 5
The variation in peak height (h) (solid symbols, continuous lines) and background level (b) (open symbols, dashed lines) expected per second for a sampling gauge of 1 mm^3 (40 mm^3 for neutrons) of Al (311) for BM16 (circles) and 16.3 (triangles) synchrotron X-rays, and for neutrons (diamonds), as a function of normalized path length based on the angles and peak widths listed in Table 4 and the calibration data acquired for the neutron (Chalk River), 16.3 (SRS) BM16 and ID31 (ESRF) synchrotron instruments.

specific instrument. Furthermore, they provide a tool for comparing different measurement strategies and for designing new instruments. The implications are investigated in part II (Withers, 2004). While this paper demonstrates the utility of calibration experiments to obtain instrument performance benchmarks, a more rigorous and systematic endeavour is required to measure and collate calibration data from instruments worldwide. To date, the background response as a function of depth has been characterized at a wide range of instruments and found in all cases examined to be exponentially dependent on the depth of the sampling gauge. This behaviour has not been explained at a fundamental level. This is necessary to modify more rigorously the predicted background level as a function of instrument configuration and component constitution and shape, and to point to ways of lowering background levels. This might require a detailed experimental and simulation study. It appears from this preliminary study that through surface depth scans in reflection, a quick and easy way of extracting the main calibration parameters (Φ_{instr} , β_0 , β_{sample}) is provided.

A comprehensive and reliable set of data measured on specific reference samples would be of great value. It would benchmark the current capability of different instruments, allowing a quantitative assessment of the improvements brought by hardware upgrades and modifications. It would enable those considering an experimental measurement scheme to evaluate the time required and the experimental feasibility. It could also be used as the basis for intelligent systems developed by facilities to enable users to plan experiments more accurately. This work has concentrated on single peak analysis. Further work is required to compare instruments that deliver complete diffraction spectra, such as time-of-flight neutron instruments and energy-dispersive X-ray instruments, with those that provide individual diffraction peaks one at a time.

This paper has demonstrated that it is not simply incident flux that determines the capability of an instrument. Often instruments based at weaker sources can shorten measurement times through intelligent use of detectors. Of equal importance when considering penetration capability is the background level. This aspect has been rather neglected at X-ray sources where the near-surface count rates are extremely high and the peak to background ratios large. As a result, there is much that remains to be done, analogous to that undertaken at neutron sources, to cut background levels and thus extend the distances into materials to which we can reasonably measure.

The concept of the feasible path length has been introduced within a rigorous framework. Because of the very high X-ray intensities available at third-generation sources compared with neutron sources, the maximum feasible path length in order to achieve 10^{-4} uncertainty is predicted to be around $6-8l_{\mu}$ for synchrotrons and around $2l_{\mu}$ for neutrons, in very good agreement with practical experience. For synchrotron

instruments, it is suggested that a peak:background criterion may be more appropriate than a maximum acceptable time, because it conveniently marks the point of diminishing returns when low signal to background seriously affects the measurement time. Its value is independent of the desired measurement accuracy. For neutrons, the peak:background ratio criterion gives longer times and greater depths than the elapsed-time criterion because of the low background signals characteristic of most neutron instruments.

This paper could not have been written without the help of all those responsible for running neutron and synchrotron strain instruments worldwide. Special thanks are owed to Drs A. Fitch, J. Wright and M. R. Daymond for special help extracting raw data, D. Hughes, A. Evans, J. Fonseca and P. A. Browne for making their experimental data available, and C. Ohms for providing data from the VAMAS TWA20 project. Helpful discussions have been had with Professor P. J. Webster and Drs M. W. Johnson, M. R. Daymond and A. Steuwer. Funding from the European Community, EPSRC and a Royal Society Wolfson Merit Award is also gratefully acknowledged.

References

- Andrews, K. W. & Johnson, W. (1959). *Brit. J. Appl. Phys.* **10**, 321–325.
- Bacon, G. E. (1975). *Neutron Diffraction*. Oxford: Clarendon Press.
- Browne, P. A. (2001). PhD thesis, University of Salford, UK.
- Chapman, D., Gmur, N., Lazarz, N. & Tomlinson, W. (1988). *Nucl. Instrum. Methods A*, **266**, 191–194.
- Elleaume, P. (1999). *Excel Macro for Computing X-ray Cross Sections*, http://www.esrf.fr/machine/groups/insertion_devices/Codes/Xray/Xray.html.
- Hirsch, P. B. (1956). *Met. Phys.* **6**, 236–339.
- Hutchings, M. T. & Windsor, C. G. (1987). *Industrial Applications. Methods of Experimental Physics*, Vol. 23C, edited by K. Sköld & D. L. Price, pp. 405–482. New York: Academic Press.
- Kocks, U. F., Tomé, C. N. & Wenk, H. R. (1998). *Texture and Anisotropy*. Cambridge University Press.
- Krawitz, A. D. (2001). *Introduction to Diffraction in Materials Science and Engineering*. New York: John Wiley.
- Santisteban, J. R., Edwards, L., Steuwer, A. & Withers, P. J. (2001). *J. Appl. Cryst.* **34**, 289–297.
- Sears, V. F. (1989). *Neutron Optics*. Oxford University Press.
- Sivia, D. S. de (1996). *Data Analysis – A Bayesian Tutorial*. Oxford University Press.
- Webster, P. J. (1996). *Mater. Sci. Forum*, **228**, 191–200.
- Webster, G. A. (2001). Editor. *Polycrystalline Materials – Determinations of Residual Stresses by Neutron Diffraction. Technology Trends Assessment*. Geneva: ISO.
- Webster, P. J. & Kang, W. (2002). *J. Neutron Res.* **10**, 93–110.
- Webster, P. J., Mills, G., Wang, X. D., Kang, W. P. & Holden, T. M. (1996). *J. Neutron Res.* **3**, 223–240.
- Webster, P. J., Wang, X. D. & Mills, G. (1996). *Strain Scanning using Neutrons and Synchrotron Radiation, ECRS 4, Clunay*, edited by S. Denis, pp. 127–134. Soc. Fr. Met. Mater.
- Withers, P. J. (2004). *J. Appl. Cryst.* **37**, 607–612.
- Withers, P. J., Daymond, M. R. & Johnson, M. W. (2001). *J. Appl. Cryst.* **34**, 737–743.